Precision Engineering 83 (2023) 216–227

Contents lists available at ScienceDirect

Precision Engineering

journal homepage: www.elsevier.com/locate/precision

A novel calibration method for angular misalignment in independently controlled fast tool servo-based diamond turning

Shigeru Tanikawa, Yusuke Sato, Jiwang Yan *

Department of Mechanical Engineering, Faculty of Science and Technology, Keio University, 3-14-1 Hiyoshi, Kohoku-ku, Yokohama, 223-8522, Japan

ARTICLE INFO

Keywords:
Diamond turning
Fast tool servo
Precise machining
Freeform surface
Ultra-precision cutting

ABSTRACT

With significant technological progress in optics fields, such as VR and 3D sensing technologies, the demand for optical components with complex shapes (e.g., freeform surfaces) has expanded significantly in recent years. Ultra-precision diamond turning is one of the common manufacturing methods used for freeform optics. There are two tool-motion mechanisms for freeform diamond turning: slow tool servo (STS), which moves the entire tool rest, and fast tool servo (FTS), which only drives the diamond tool. In particular, high-frequency and long-stroke FTS units driven by a separate control system from the machine tool controller have recently been developed as a new trend in FTS-based diamond turning. However, this type of independent FTS control system causes a time delay between the machine tool instruction and the FTS tool motion. Even a millisecond-scale time delay can cause a considerable angular misalignment owing to the high rotation rate of the spindle, resulting in a micron-scale form error on the workpiece surface. In this paper, a novel method for precisely measuring the time delay from the machined workpiece surface and compensating for the misalignment based on the measured time delay was proposed. To measure the time delay, spherical dimples were machined on the workpiece surface by using STS and FTS. Subsequently, the angular misalignment and time delay were obtained by comparing the measured surface profiles at specific positions of the spherical dimples. Thus, the time delay can be measured with microsecond-scale accuracy. Based on the measured time delay, the shifted tool position along the spindle axis by the time delay was compensated to the ideal tool position by considering the cutting velocity. Consequently, the angular misalignment was completely eliminated, and submicron-level form accuracy was achieved. This calibration method of angular misalignment for an independent FTS unit is expected to significantly improve the accuracy of ultra-precision machining of freeform optics.

1. Introduction

Technological developments in optical element manufacturing in recent years have enabled the fabrication of lenses, mirrors, and molds with complex shapes, such as aspherical and freeform surfaces [1–3]. Freeform lenses can achieve high optical efficiency and reduce the number of optical components owing to the flexibility of their shape design. High-precision freeform lenses have many advantages over spherical and aspherical lenses, such as cost reduction, downsizing and simplification of the optical system, expansion of the field of view, and improvement of imaging resolution [4–6]. Freeform lenses have been used as components of head-mounted displays in VR and AR technologies in recent years [7–9]. Improvements in the accuracy and production efficiency of freeform lenses can contribute more to these fields.

The optical performance of freeform lenses generally depends on their form accuracy and surface properties [10,11]. Therefore, machining methods for freeform lenses that achieve a higher form accuracy and better surface properties are required. Lithography and ultra-precision cutting are main processing methods for freeform lenses [12–14]. However, lithography is only useful for certain specific materials, and the achievable feature size is small. In addition, the consistency of machining accuracy and process controllability is poor compared to ultra-precision cutting [15,16].

Ultra-precision cutting for the fabrication of freeform surfaces is commonly performed by milling and turning diamond tools [17,18]. In ultra-precision milling, material removal is conducted by moving a rotating tool on a fixed workpiece, and the tool raster motion is controlled to match the designed lens shape. In general, rater milling is time-consuming compared to turning [19]. Freeform surface turning is performed by driving a diamond tool using slow tool servo (STS) or fast

* Corresponding author.
E-mail address: yan@mech.keio.ac.jp (J. Yan).

https://doi.org/10.1016/j.precisioneng.2023.06.010
Received 12 November 2022; Received in revised form 10 March 2023; Accepted 17 June 2023
Available online 19 June 2023

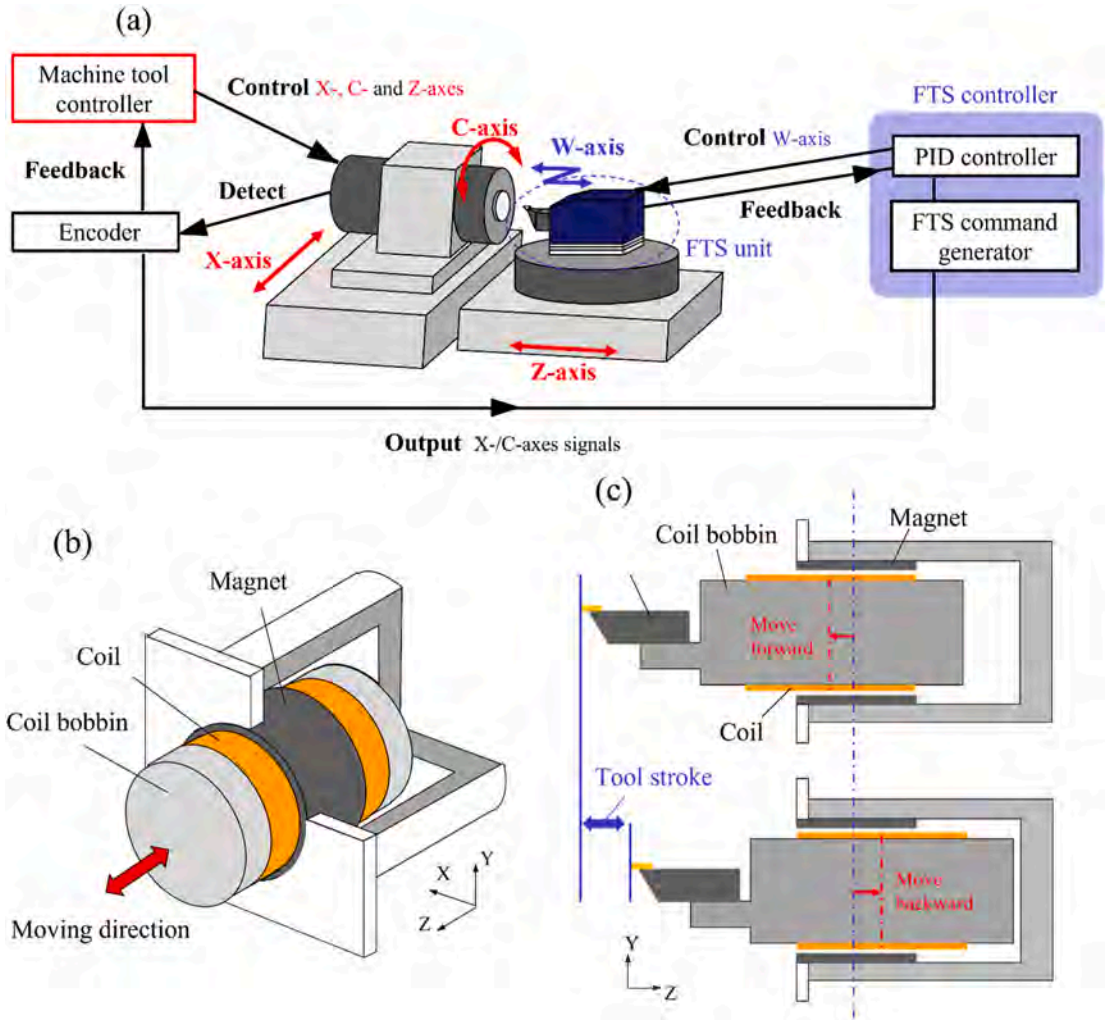

Fig. 1. (a) Machining control flow of FTS-based diamond turning and (b) overview and (c) side view of voice coil in the FTS unit.

tool servo (FTS) mechanisms [20]. In STS-based diamond turning, the tool rest of a lathe moves back and forth during workpiece rotation, where the large mass of the tool rest causes significant following (or tracking) errors during machining. To reduce the following error, the oscillation frequency of the tool rest must be extremely low. However, in FTS-based diamond turning, the FTS unit is mounted on the tool rest, and only the tool, which has a small mass, is moved back and forth with negligible following errors [16,21,22]. Consequently, the oscillation frequency of an FTS is much higher than that of an STS, which enables very high machining efficiency.

Conventionally, piezoelectric elements have been used to realize FTS tool motion, where the stroke of the tool oscillation is limited to a few tens of microns. In recent years, as a new trend, independent FTS units equipped with voice coil-driven air bearings have been developed [23–25]. Using a voice coil, the driving stroke was improved to a few millimeters while maintaining the same response performance as that of a piezoelectric FTS unit [26]. Ultra-precision diamond turning using an independent FTS unit equipped with a voice coil enables the high-speed and high-precision machining of high-aspect-ratio freeform lenses with steep surfaces.

However, the back-and-forth movement of the tool in the independent FTS unit is controlled by a dedicated control system that is separate from the machine-tool controller [26,27]. Therefore, there is a time delay between the two control systems because the FTS tool movement is controlled after obtaining the instruction signal data of the machine tool controller. Because this time delay causes an angular misalignment of the spindle rotation and, in turn, induces a form error on the workpiece, there is an urgent need to precisely measure the time delay and compensate for the misalignment.

In this study, a novel calibration method for angular misalignment in independently controlled FTS-based diamond turning was proposed. In this method, the angular misalignment and time delay were measured by comparing the surface profiles at specific positions of a set of spherical dimples using STS and FTS, respectively. The effectiveness of the proposed calibration method was validated by measuring the time delay and compensating for it in a series of cutting experiments.

2. Theory and method

2.1. System control flow

As shown in Fig. 1, the X-, C-, and Z-axes are driven by the machine tool controller, and the W-axis is driven by an independent FTS unit controller in accordance with the movement of the X- and C-axes. The diamond tool is fixed by the FTS unit and moved along the W-axis by an independent control system, which realizes fast oscillation motion. The voice coil inside the FTS unit illustrated in Fig. 1(b) realizes a fast and precise movement. As shown in Fig. 1(c), the electric current in the coil generates a magnetic field and the coil bobbin moves back and forth by the magnetic action of the generated magnetic field and the attached magnet.

Fig. 2 illustrates the control program flow of FTS turning.

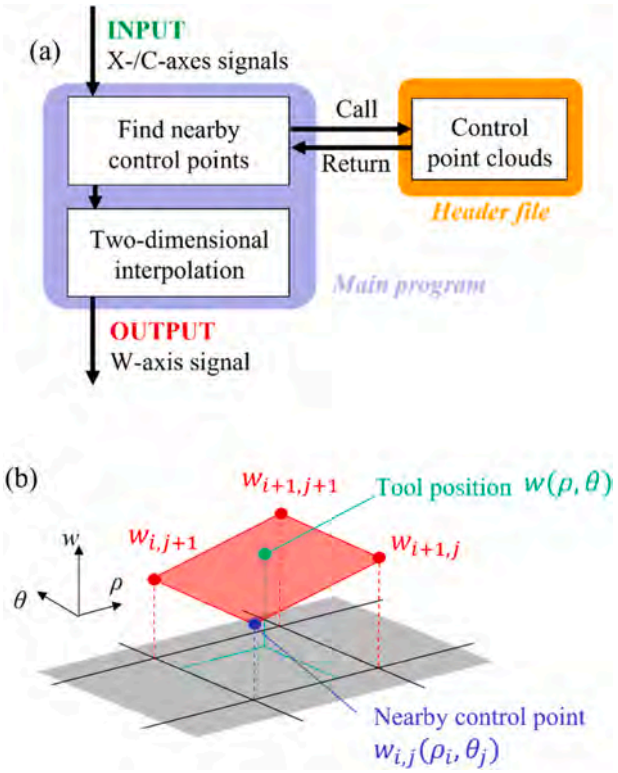

Fig. 2. (a) Overview of the FTS tool-path program and (b) determination of the W-axis tool position by bilinear interpolation.

Independent FTS-based diamond turning requires two machining programs: a program to control the X-, Z-, and C-axes (toolpath program for STS: TPS) and a program to move the diamond tool installed on the FTS unit along the W-axis following the movement of the X- and C-axes (toolpath program for FTS: TPF). The tool position coordinates of the X-, C-, and Z-axes controlled by the TPS were output to the control system of the independent FTS unit. TPF calculates the tool position along the W-axis based on the output tool position coordinates during processing. In TPF, the main program determines the W-axis coordinate value by referring to the control point clouds of the header file based on the designed surface and conducting two-dimensional interpolation, as shown in Fig. 2 (a). After obtaining the X- and C-axis tool position values, a search was performed for the four points data closest to the tool position in the control point cloud data. Then, two-dimensional interpolation is performed based on the searched points to determine the W-axis command tool position w, as shown in Fig. 2(b).

$$w=(1-t)(1-u)w_{i,j}+t(1-u)w_{i+1,j}+tuw_{i+1,j+1}+(1-t)uw_{i,j+1}, \tag{1}$$

where t and u cover a range between 0 and 1 and are given as

$$t=\frac{(\rho-\rho_i)}{(\rho_{i+1}-\rho_i)}, \tag{2-a}$$

$$u=\frac{(\theta-\theta_i)}{(\theta_{i+1}-\theta_i)} \quad . \tag{2-b}$$

Based on the calculated W-axis coordinate value, the PID controller of the FTS unit drives the diamond tool to move accurately and at high speed. Thus, independent FTS-based diamond turning can achieve the fast and precise machining of a freeform surface.

2.2. Angular misalignment caused by time delay

Although independent FTS-based diamond turning allows for efficient manufacturing, the problem is that a time delay occurs between the machine tool controller and the control system of FTS unit. In high-speed FTS machining, even a little time delay can cause a large angular misalignment. The effects of the spindle rotation rate s and time delay Δt on the machining angle deviation $\Delta\theta$ can be calculated using the following equation:

$$\Delta\theta=6s\Delta t \tag{3}$$

If the rotation rate and time delay are 500 rpm and 100 μs, respectively, an angular misalignment of 0.3° occurs. Assuming that the workpiece size is φ60, an angular misalignment of 0.3° causes a maximum machining position misalignment of 157 μm. This FTS-induced angular misalignment leads to a higher form error proportional to the size of the workpiece.

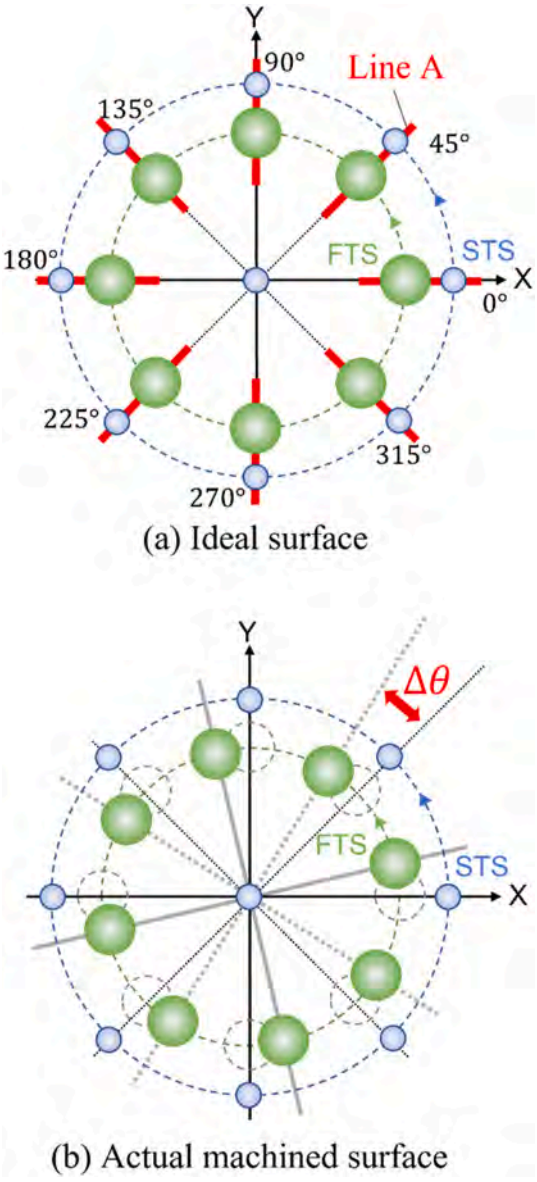

Fig. 3. (a) Ideal surface of the proposed designed surface to measure time delay. (b) Actual machined surface where only the FTS spherical dimples were shifted to the rotation direction by time delay.

2.3. Surface design for time delay measurement

A surface was designed for STS and FTS machining to accurately measure the time delay from the machined sample surface (Fig. 3). The outer small and large spherical dimples were machined using STS and

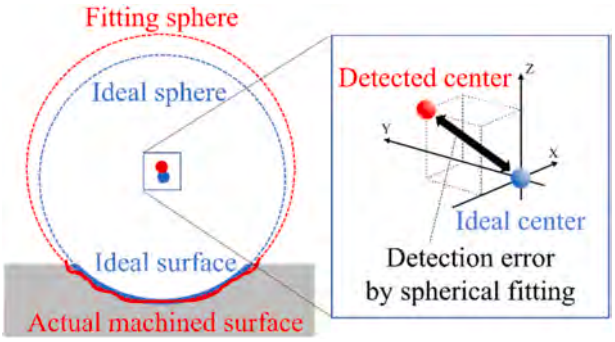

Fig. 4. Schematic diagram of misalignment between the ideal spherical dimple center and center position detected by sphere fitting of the actual machined surface.

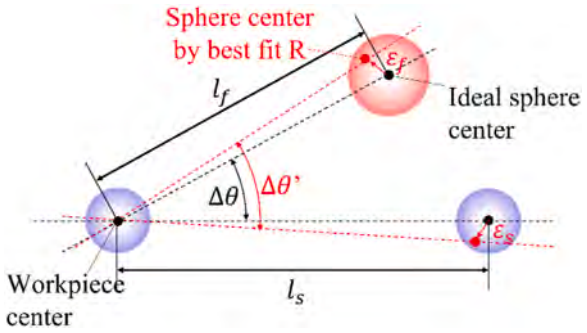

Fig. 5. Schematic diagram of the shifted angle change by the spherical fitting error.

FTS, respectively. The designed surface consists of spherical dimples machined by FTS and STS at an angular space of 45° in the outer region of the workpiece and a spherical dimple machined by STS in the workpiece center. On the designed surface, the spherical dimples were aligned in line A, as illustrated in Fig. 3(a). However, on the actual workpiece surface, only the FTS spherical dimples were shifted in the rotational direction owing to the time delay, as illustrated in Fig. 3(b). The angular misalignment of the FTS spherical dimples can be calculated by comparing the positions of the STS spherical dimples. When the position coordinates of the spherical dimples in the workpiece center and the outer region machined by FTS and STS are expressed as (x_0, y_0), (x_f, y_f), and (x_s, y_s), respectively, the angular misalignment of the FTS-machined spherical dimple can be obtained as follows:

$$\Delta\theta = \tan^{-1}\left(\frac{y_f - y_0}{x_f - x_0}\right) - \tan^{-1}\left(\frac{y_s - y_0}{x_s - x_0}\right), \tag{4}$$

where $\Delta\theta$ is the angular misalignment of the FTS spherical dimple position compared with the center and STS spherical dimple positions. Based on the calculated angular misalignment, the time delay is obtained as follows:

$$\Delta t = \frac{\Delta\theta}{6s} \quad . \tag{5}$$

By conducting these calculations, the average shifted angle and time delay values for independent FTS-based diamond turning can be obtained.

2.4. Spherical surface fitting

To accurately calculate the time delay, the center of the machined spherical dimples must be precisely detected. To determine the center position of each spherical dimple from the machined workpiece surface, the shape of the measured spherical dimples was acquired as point cloud data, and spherical fitting was performed using the least-squares method. The objective function for the spherical fitting to the point cloud data of the measured spherical dimples is as follows:

$$S(x_c, y_c, z_c, r) = \sum_{i=1}^{m} \left((x_i - x_c)^2 + (y_i - y_c)^2 + (z_i - z_c)^2 - r^2\right)^2, \tag{6}$$

where (x_i, y_i, z_i) is each measurement points with numbers of m. (x_c, y_c, z_c) and r are the detected center positions and best-fit curvature values of the fitting result, respectively. When the objective functions $S(x_c, y_c, z_c, r)$ are minimized, the optimal center position and radius of the fitting sphere can be obtained. The objective function in Equation (6) is expressed as follows:

$$S(x_c, y_c, z_c, r) = \sum_{i=1}^{m} \left(x_i^2 + y_i^2 + z_i^2 - X_c x_i - Y_c y_i - Z_c z_i - R\right)^2, \begin{cases} X_c = 2x_c \\ Y_c = 2y_c \\ Z_c = 2z_c \\ R = r^2 - x_c^2 - y_c^2 - z_c^2 \end{cases} . \tag{7}$$

The value of each variable that minimizes the objective function is determined by finding a solution that is zero through partial differentiation of each variable, as in the following equation:

$$\frac{\partial S}{\partial R} = \frac{\partial S}{\partial X_c} = \frac{\partial S}{\partial Y_c} = \frac{\partial S}{\partial Z_c} = 0 \quad . \tag{8}$$

From Equations (7) and (8), the partial differentiation of each variable can be summarized by the following matrix:

$$\begin{bmatrix} R \\ X_c \\ Y_c \\ Z_c \end{bmatrix} = \begin{bmatrix} m & \sum x_i & \sum y_i & \sum z_i \\ \sum x_i & \sum x_i^2 & \sum x_i y_i & \sum x_i z_i \\ \sum y_i & \sum x_i y_i & \sum y_i^2 & \sum y_i z_i \\ \sum z_i & \sum x_i z_i & \sum y_i z_i & \sum z_i^2 \end{bmatrix}^{-1} \begin{bmatrix} \sum (x_i^2 + y_i^2 + z_i^2) \\ \sum x_i (x_i^2 + y_i^2 + z_i^2) \\ \sum y_i (x_i^2 + y_i^2 + z_i^2) \\ \sum z_i (x_i^2 + y_i^2 + z_i^2) \end{bmatrix} . \tag{9}$$

The center position of the spherical dimple and the radius of curvature of the best fit can be obtained by performing the calculations in Equation (9) on the measured point cloud data and deriving the values of R, X_c, Y_c, and Z_c.

2.5. Measurement accuracy of time delay

As shown in Fig. 4, the center coordinates of each sphere can be detected from the machined workpiece surface via spherical fitting.

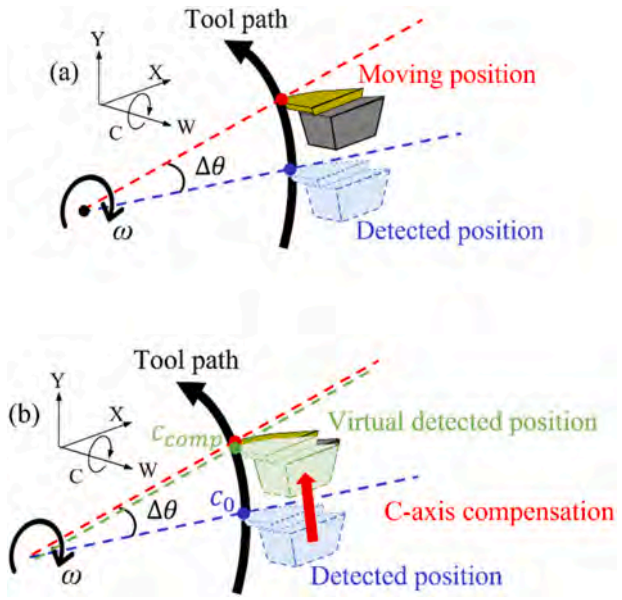

Fig. 6. (a) Detected tool position and moving tool position. (b) Virtual detection position by time delay compensation before determining the W-axis coordinate value.

However, in the actual machined workpiece surface, the sphere center coordinates detected by the fitting process are slightly shifted from the ideal sphere center coordinates owing to the form error of the actual machined workpiece surface. These sphere-center detection errors eventually lead to time delay measurement errors. Sphere-center detection errors occur at the FTS and STS dimples in the outside region of the workpiece (Fig. 5). For spherical dimples at the workpiece center, the sphere center detection error is close to zero because the form error appears on the axis object based on the center of rotation. These sphere center detection errors cause changes in the positional relationships of the FTS and STS spherical dimples, leading to errors in the time delay measurement. Because the sphere center detection error is related to the measurement error of the time delay, the influence of the detection error must be suppressed by adjusting the dimple size and arrangement.

The measurement error of the time delay, Δt_ε, caused by the sphere center detection error can be expressed (Fig. 5).

$$\Delta t_\varepsilon = \frac{\Delta\theta' - \Delta\theta}{6s}, \tag{10}$$

where $\Delta\theta'$ is the amount of shift in the cutting direction of the FTS dimple when a sphere center detection error occurs. In this case, the maximum possible value of the measurement error, $\Delta t_{\varepsilon-max}$, is expressed as follows:

$$\Delta t_{\varepsilon-max} = \frac{\sin^{-1}\left(\frac{\varepsilon_f}{l_f}\right) + \sin^{-1}\left(\frac{\varepsilon_s}{l_s}\right)}{6s}, \tag{11}$$

where l_f and l_s are the distances of the spherical dimples of FTS and STS from the center spherical dimple, respectively, and ε_f and ε_s are the detection errors of spherical dimples machined by FTS and STS, respectively. The above equation shows that the maximum measurement error $\Delta t_{\varepsilon-max}$ is determined by the five variables: l_f, l_s, ε_f, ε_s, and s. By considering these five variables in determining the detailed conditions, a highly accurate measurement of time delays can be achieved.

2.6. Time delay compensation

By correcting the measured time delay during machining using an independent FTS unit, ultra-precision machining without angular misalignment is possible. To compensate for the time delay, a program that redefines the detected C-axis coordinate value of the tool position based on the measured time delay was applied to the FTS controller. As shown in Fig. 6(a), before the time delay compensation, the detected tool position and moving tool position are different, and the W-axis coordinate value is calculated based on the detected tool position. Therefore, the calculated tool position at the detected position is shifted to a different position (Moving position in Fig. 6(a)), which is the cause of the angular misalignment. However, by compensating for the detected C-axis tool position according to the following equation, the exact W-axis coordinate value at the position where the tool starts to move can be calculated:

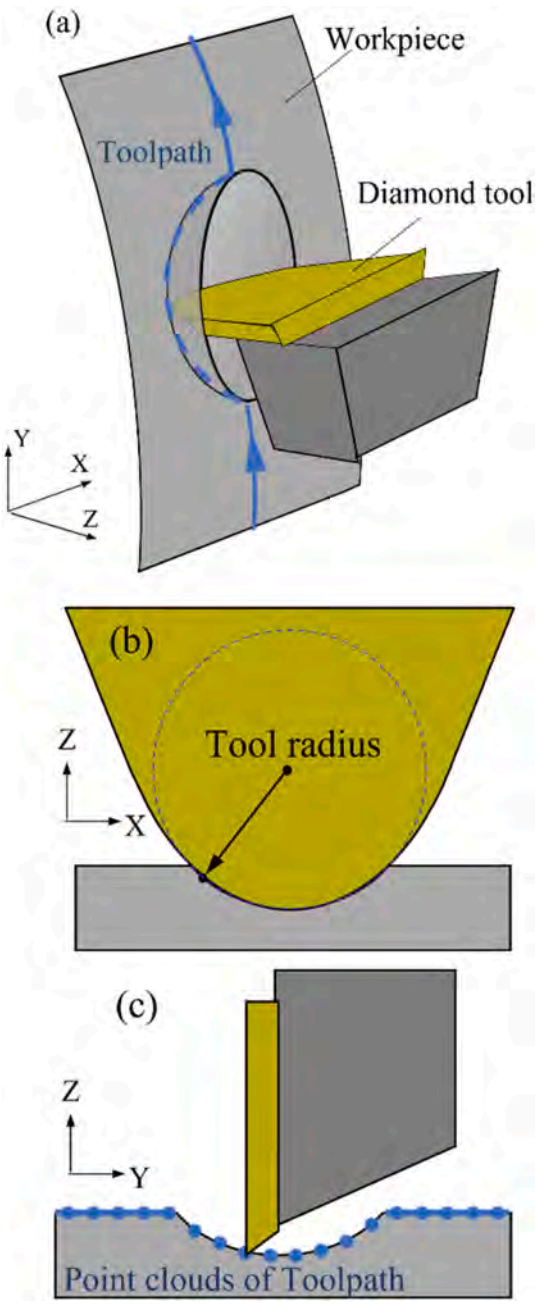

Fig. 7. (a) Overview, (b) front view, and (c) side view of spherical dimple machining by scooping cutting.

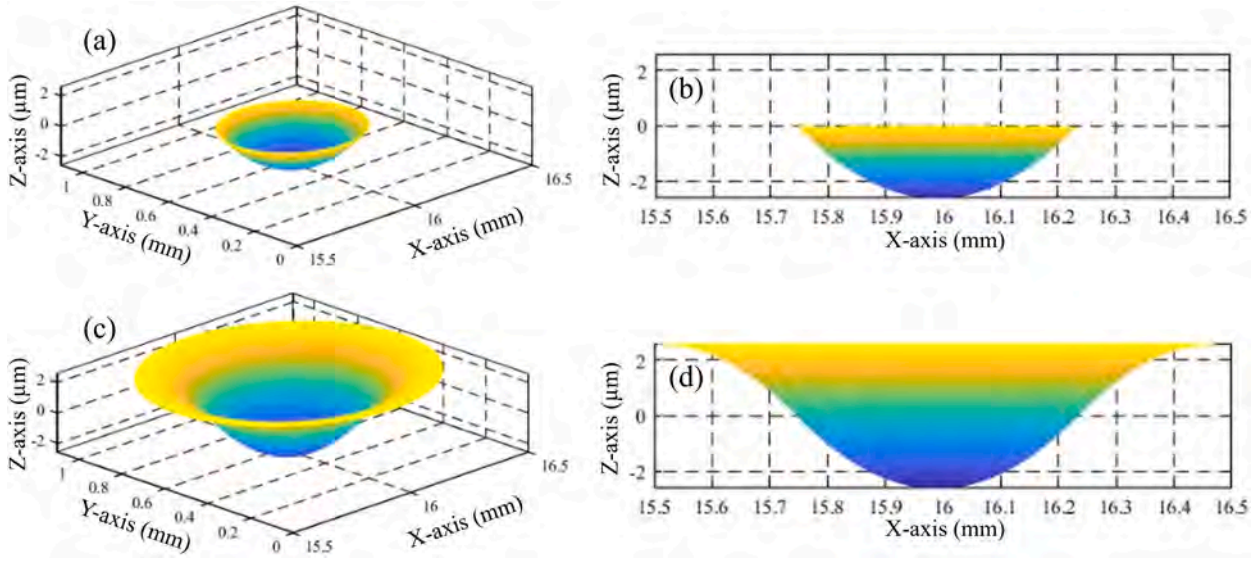

Fig. 8. (a) Overview and (b) side view of simple spherical dimple and (c) overview and (d) side view of the torus-shaped spherical dimple for tool acceleration aiding.

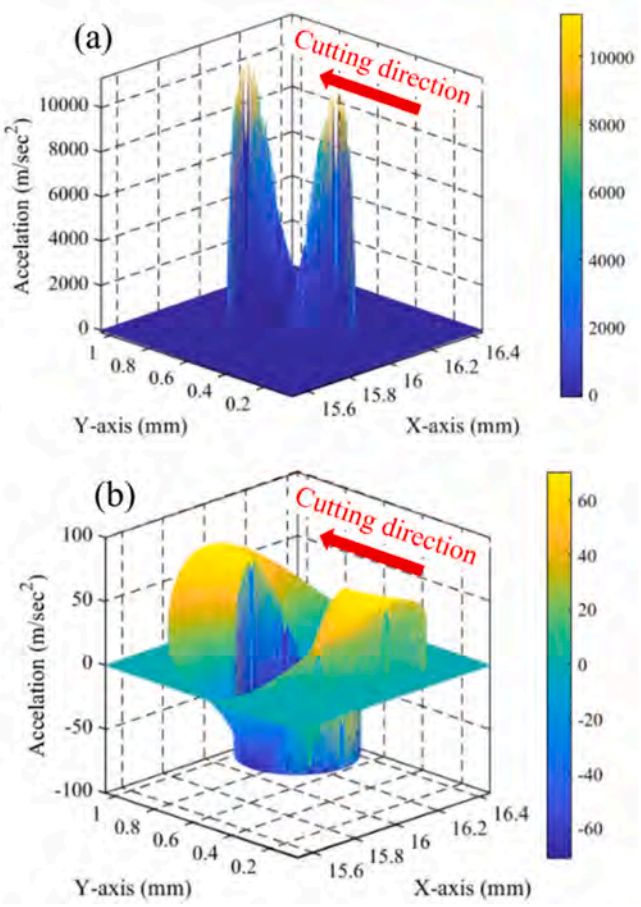

Fig. 9. Simulation results of tool acceleration of (a) simple spherical dimple (Fig. 8(a) and (b)) and (b) spherical dimple with torus shape for tool acceleration aiding (Fig. 8(c) and (d)).

$$c_{comp} = c_o + \omega \Delta t, \tag{12}$$

where c_{comp} and c_o are the values before and after compensation of the detected C-axis tool position, respectively, and ω is the angular velocity of the spindle rotation.

Table 1
Simulation conditions of tool acceleration.

Simulation conditions	Value
Cutting parameters	
Spindle rotation (rpm)	500
Cutting area, X-axis (mm)	10
Cutting area, C-axis (°)	5
Designed form parameters	
Curvature of spherical dimple (mm)	10
Depth of spherical dimple (μm)	2.6
Radius from the center of torus (μm)	456
Cylindrical ring width radius of torus (mm)	10
Height of torus (μm)	2.6

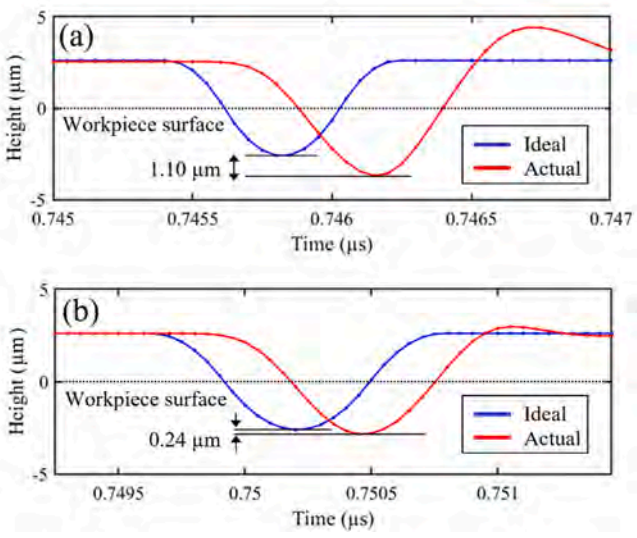

Fig. 10. Sampling data of ideal and actual tool motion at (a) 6.0 mm and (b) 11.3 mm spherical dimple curvatures.

By applying this correction to the detected C-axis coordinates, a virtually detected position is set where the tool starts to move, as shown in Fig. 6(b). Further, the command generator calculates the W-axis coordinate value based on this virtual detected position.

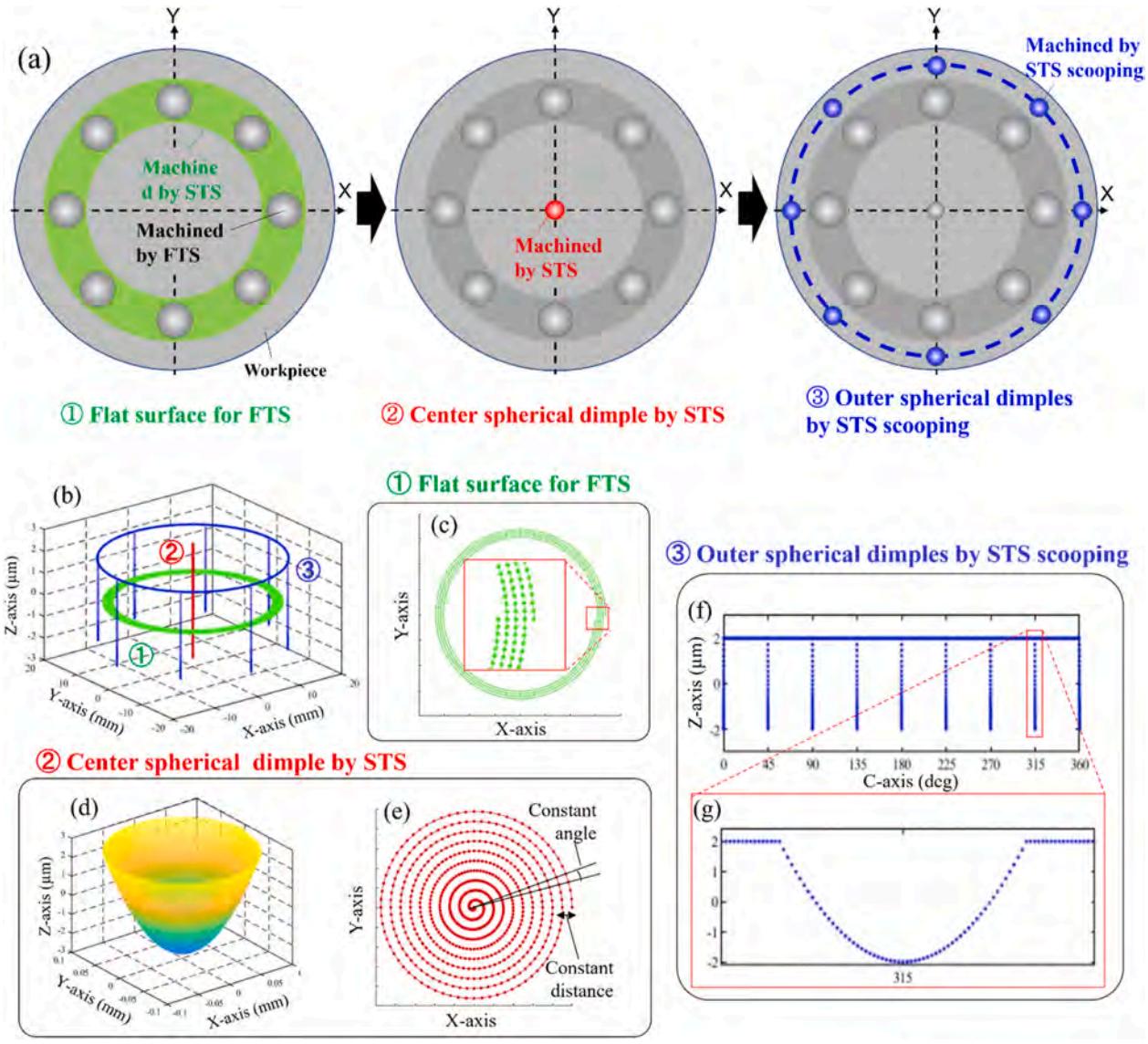

Fig. 11. (a) Schematic diagram of procedure for machining each spherical dimple; (b) Overview of TPS to machine the proposed designed surface; (c) flat surface cutting for FTS machining; (d) overview and (e) point cloud data arranged by isometric method for the center spherical dimple by STS machining; (f) point cloud data of one rotation for scooping cutting; and (g) enlarged view of machining for a spherical dimple.

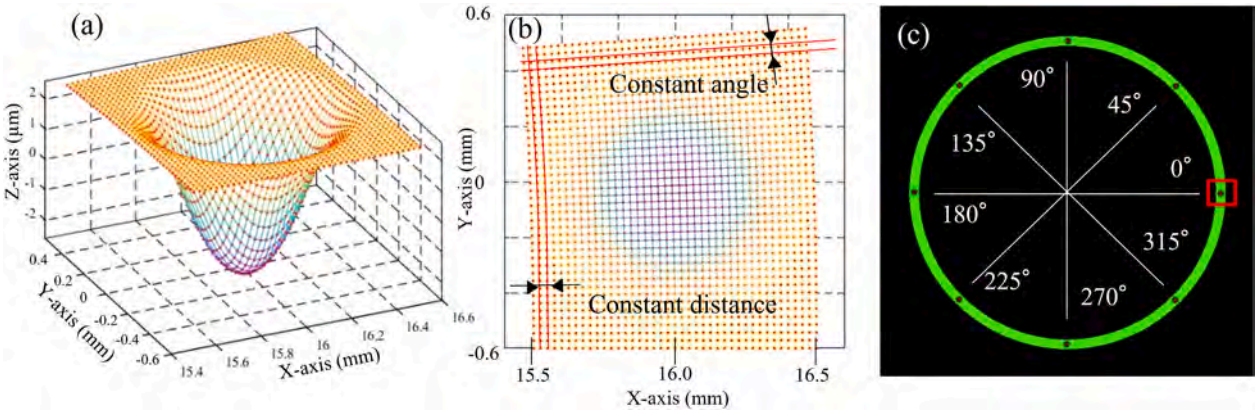

Fig. 12. (a) Overview and (b) arranged point cloud data of a single spherical dimple designed to be placed at a constant angle and distance. (c) Overview of TPF for machining eight outer spherical dimples by FTS machining.

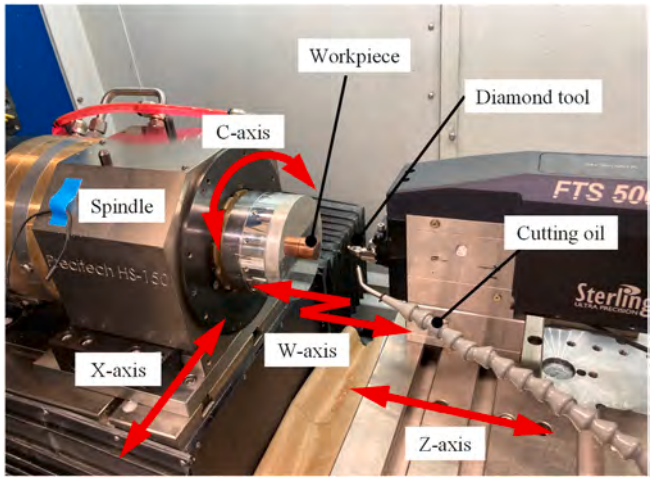

Fig. 13. Photograph of the main section of the experimental setup for FTS-based diamond turning.

Table 2
Cutting conditions.

	FTS	Center	STS
Cutting parameters			
Spindle rotation rate (rpm)	500	25	0.4
Feed rate (mm/s)	0.001	0.001	0
	Rough: 2.6	Rough: 2.6	
Depth of cut (μm)	Fine: 1	Fine: 1	Fine:1
Radius of cutting area (mm)	15~17	0~0.1	18
Coolant	Oil (kerosene) mist		
Cutting tool			
Tool material	Single-crystal diamond		
Nose radius (mm)	0.19		
Rake angle (°)	0		
Clearance angle (°)	7		
Workpiece			
Material	Oxygen-free copper		
Diameter (mm)	50		

Table 3
Designed form conditions.

	FTS	Center	STS
Spherical dimple			
Curvature radius (mm)	11.3	1.13	0.19
Depth (μm)	2.6	2.6	1
Radius of location (mm)	16	0	18
Number of dimples	8	1	8
Torus shape			
Radius from the center (μm)	485	–	
Radius of cylindrical ring width (mm)	11.3		
Height (μm)	2.6		

2.7. Scooping cutting method

As described in Section 2.5, the error in determining the center position of the spherical dimple using the fitting process has a significant effect on the measurement accuracy of the time delays. Therefore, it is necessary to reduce the detection error. To suppress the detection error, spherical dimples must be machined as small as possible while maintaining high accuracy. To machine such spherical dimples, a scooping cutting method was proposed in this study. When an arc-nosed tool is used, a small spherical dimple can be machined by precisely moving the tool in the Z-axis direction in line with the tool radius (Fig. 7). Each cutting depth z_n for scooping cutting at an equal angle θ_{cons} is determined as follows:

$$z_n(c) = r_{curv} - d - \sqrt{{r_{curv}}^2 - \left(\frac{r_{pos}(c\pi - \theta_{cons}(n-1))}{180}\right)^2},\ n = 1, 2\cdots\left(\frac{360}{\theta_{cons}} + 1\right), \tag{13}$$

where r_{curv}, r_{pos}, d, and c are the curvature radius of the spherical dimple, scooping position radius from the center of the workpiece, maximum depth of the spherical dimple, and c-axis angle position, respectively. Each z_n value was set to zero when the value was greater than zero, and the c-axis value was outside the range of the following equation:

$$-r_{curv} < \frac{r_{pos}\pi}{180}(c - \theta_{cons}(n-1)) < r_{curv} \quad . \tag{14}$$

By determining the Z-axis coordinate value that circle on the surface of the workpiece along the introduced flow, it is possible to perform scooping cutting of spherical dimples placed at equal angles.

The spindle rotation rate must be reduced to process spherical dimples accurately via scooping cutting. Because the spindle rotation rate also affects the accuracy of the time delay measurement, as described in Section 2.5, this scooping method cannot be used for spherical dimples machined by FTS, which requires high-speed rotation. Therefore, scooping cutting was applied to machine the outer eight STS spherical dimples.

3. Experimental procedures

3.1. Decision of FTS machining conditions

To precisely measure the time delays by machining the proposed surface in Section 2.3 with FTS-based diamond turning, the cutting conditions and designed form parameters were selected. In particular, the spindle rotation rate, distance from the center of the workpiece where the STS and FTS spheres are placed, and radius of curvature of each sphere affect the measurement accuracy in time delay measurements, as described in Section 2.5.

First, the amount of spindle rotation during the FTS machining was determined. From Equation (3), the amount of angular shift in the cutting direction owing to the time delay is proportional to the amount of spindle rotation, assuming that the time delay is constant. When the sphere center detection error is constant, a high spindle rotation rate reduces the time delay measurement error from Equations (10) and (11). In this study, to utilize the time delay measurement results for other general machining of FTS, a spindle rotation rate of 500 rpm, which is widely used for FTS machining with a high spindle rotation rate, was set as the spindle rotation rate for the machining of FTS spherical dimples [22].

After the rotation rate was determined, the spherical dimple design parameters were derived to reduce the sphere center detection error. The small curvature radius of the spherical dimple reduces the spherical fitting errors. However, too much small spherical dimples cannot be machined precisely because the tool cannot follow them during high-speed rotation, such as 500 rpm. In particular, if the tool is moved according to the designed spherical dimple shape shown by the theoretical 3D topographies in Fig. 8(a) and (b), a sudden change in the tool acceleration occurs at the beginning and end of the cutting, resulting in a large following error. To suppress this sudden change in tool acceleration, a torus shape was applied to the spherical dimples machined by FTS, as shown in Fig. 8(c) and (d). The general torus shape can be expressed as follows:

$$\left(\sqrt{x^2 + y^2} - r_d\right)^2 + z^2 = {r_w}^2, \tag{15}$$

where r_d and r_w are the radii from the center of the torus shape and the cylindrical ring width radius, respectively. By combining the torus shape with the spherical dimple shape as a tool aid, the change in tool acceleration and tool-following error is expected to be significantly reduced.

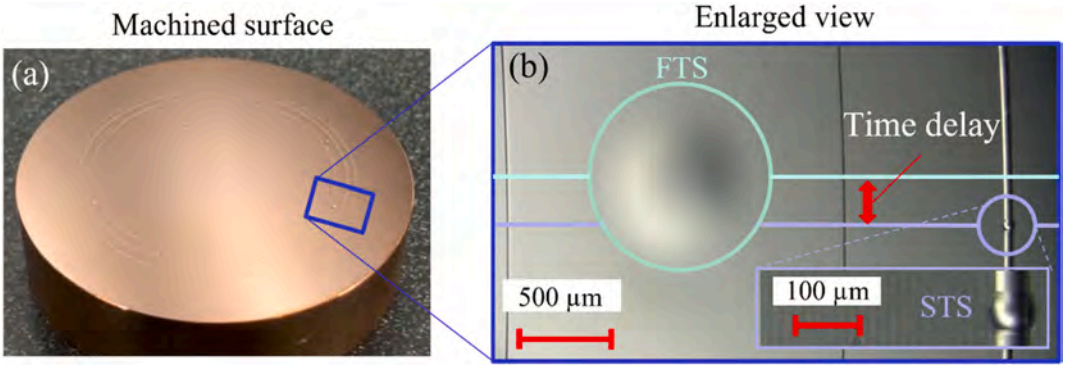

Fig. 14. Observation and measurement results of a machined surface: (a) optical image and (b) enlarged view by laser microscopy.

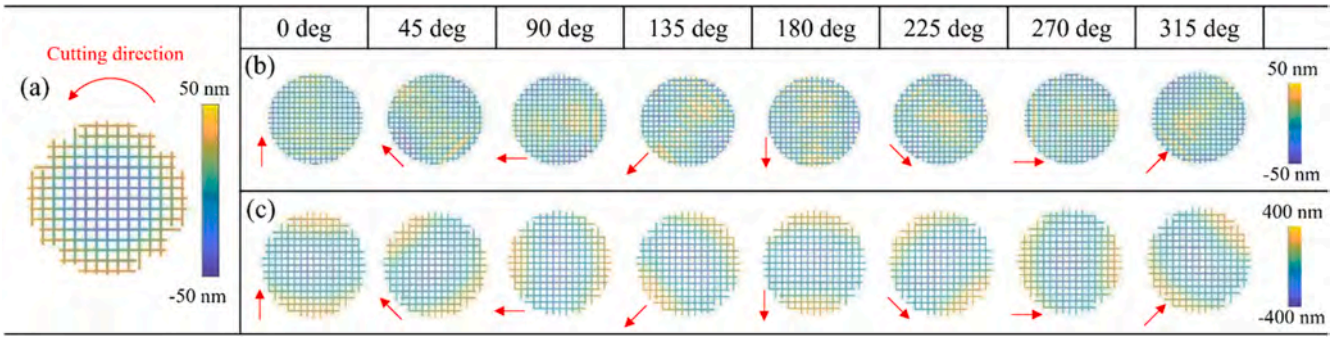

Fig. 15. Form error map of the (a) machined center spherical dimple by STS and eight outer spherical dimples machined by (b) STS and (c) FTS.

Fig. 9 shows the simulation results of the tool acceleration for a simple spherical dimple shown in Fig. 8(a) and (b), and a spherical dimple with a torus shape shown in Fig. 8(c) and (d). The simulation conditions are listed in Table 1. The results presented in Fig. 9 show that the range of maximum change in acceleration is reduced from 11363 m/ s^2 to 141 m/ s^2 (98.8% reduction) when the torus shape is applied, confirming that the torus shape is appropriate as a tool aid.

The radius of curvature of the spherical dimple was selected by comparing the obtained tool following errors of various radii of curvature with a fixed depth of the sphere dimple at 2.6 μm. The following errors were obtained when the tool passed through the center of the spherical dimple, where the tool motion was the largest. The two acquired errors at curvature radii of 6 mm and 11.3 mm are shown in Fig. 10. The blue line in the graphs shows the ideal tool path calculated via the TPF, and the red line shows the actual tool path moved by the PID controller of the independent FTS unit. When the radius of curvature was set to 6 mm, the spherical dimple was too small for the tool to follow at a high-speed rotation of 500 rpm, and the actual tool motion was significantly different from the commanded motion, resulting in an overrun of 1.10 μm, as shown in Fig. 10(a). However, when the radius of curvature was set to 11.3 mm, the accuracy of the tool motion moved by the tool path command improved, as shown in Fig. 10(b). The overrun was reduced to 0.24 μm, which was less than one-tenth of the 2.6 μm depth of cut. From the error data, the radius of curvature of the spherical dimple to be machined with FTS in this study was determined to be 11.3 mm.

3.2. Toolpath program

The machining procedure for each kind of spherical dimple is illustrated in Fig. 11(a). First, a flat surface is machined using STS, while spherical dimples are machined using FTS. Next, a spherical dimple is machined in the center of the workpiece using STS. Finally, the outer spherical dimples are machined using STS scooping.

The prepared point cloud data for the three TPS toolpath programs to machine each spherical dimple are summarized in Fig. 11(b). Fig. 11(c) shows the STS toolpath program for the area where a spherical dimple was machined with FTS. The turning machine moves according to this point cloud, with the entire tool rest moving evenly in the X-axis direction while the spindle rotates, and the Z-axis movement remains constant at the zero position. The turning machine controls the C-, X-, and Z-axes based on the point cloud data, and the tool position of each axis of the tool rest is detected in real time by encoders and output to the independent FTS unit, which determines the W-axis coordinate value to machine the design shape based on the FTS tool-path program described below. Fig. 11(d) and (e) show the toolpath program for the sphere to be machined in the center of the workpiece. The toolpath program consisted of point cloud data arranged equiangularly in a spiral shape, with a constant horizontal width of the point cloud of 1 μm and a constant angle of 1°. The sphere was machined by moving the tool according to the Z-axis value of the point cloud data. The point cloud data were corrected based on tool radius compensation to obtain a more precise spherical dimple shape of the machined surface [28,29]. Fig. 11(f) and (g) show the toolpath program for machining STS spherical dimples via scooping cutting. Spherical dimples can be machined by scooping cutting, in which the tool moves according to the same curvature as the tool radius at an angular space of 45°, using the point cloud data for one rotation.

The TPF was created using C language and point cloud data for FTS machining. The independent FTS unit used in this study allows tool movement to be controlled by the C language. In the widely used spiral point cloud data with constant horizontal width and angle, the density of the point cloud becomes sparser toward the outside, and it is difficult to process precise spherical dimples using constant angle point cloud data. To process a spherical dimple with high form accuracy at 16 mm along the X-axis, point cloud data representing only one spherical dimple was prepared, as shown in Fig. 12 (a) and (b). This spherical dimple was processed at an angular space of 45° by a C language program, as shown

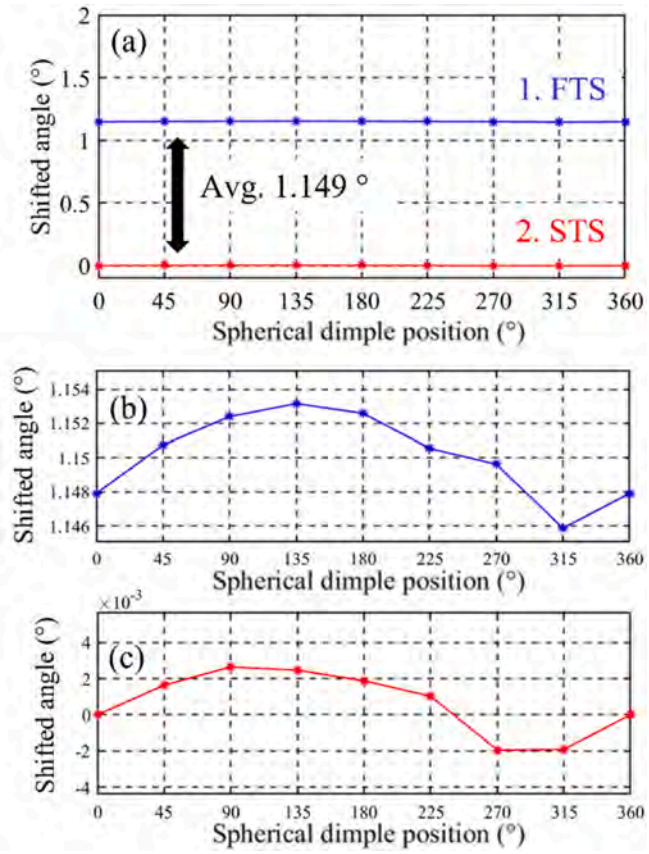

Fig. 16. (a) Measurement results of the shifted angle from the ideal position based on the detected center position of 0° and each enlarged graph of (b) FTS and (c) STS.

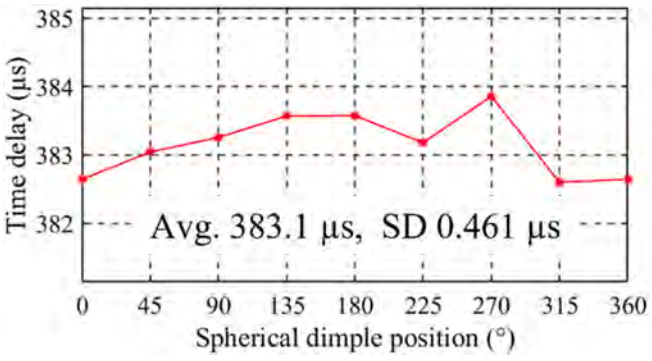

Fig. 17. Time delay calculation results based on the measured shifted angle.

in Fig. 12(c). To machine a spherical dimple at an angular space of 45° using the prepared point cloud data of a single spherical dimple, the W-axis coordinate value was determined based on the excess value of the detected C-axis value divided by 45. The spherical dimples are processed by referring to the prepared point cloud data only when the post-processing C-axis value is less than 4°. When the value is greater than 4°, the program is set the W-axis coordinate value to 2.6 μm, which is the maximum height value of the point cloud data. When the X-axis value is outside the point cloud data range ($x < 15.5$ mm and 16.5 mm $< x$), the W-axis coordinate value is set to zero.

3.3. Cutting setup and conditions

The time delay was measured and corrected by machining the designed surface for the fast tool servo FTS-5000 (AMETEK Precitech Inc.) attached to the NanoformX (AMETEK Precitech Inc.) ultra-precision diamond turning machine (Fig. 13). This independent FTS unit acquires the position value of the tool moved by NanoformX during machining and determines the W-axis coordinate value based on TPF. Linear motors that can be controlled by a PID controller are used to move the tool at a high speed and with high accuracy relative to the calculated amount. The FTS unit used in this study had a maximum stroke of 5 mm and maximum frequency of 440 Hz. When machining the FTS and STS spheres, the Z- and W-axis were fixed, respectively. A round-nosed single-crystal diamond tool with a nose radius of 0.19 mm, rake angle of 0°, and clearance angle of 7° was used in the experiment. An oxygen-free copper cylinder with a diameter of 50 mm was used as the workpiece. The designed surface parameters and conditions of the cutting experiment are summarized in Tables 2 and 3. The cutting experiment was conducted twice: before and after the time delay compensation. In the first experiment, the time delay was measured, and the compensation process described in Section 2.6 was applied in the second experiment based on the measured time delay. A digital microscope VHX1000 (Keyence Co., Ltd.) and an ultrahigh accurate 3-D profilometer UA3P 5000H (Panasonic Co., Ltd.) were used to measure the machined surface.

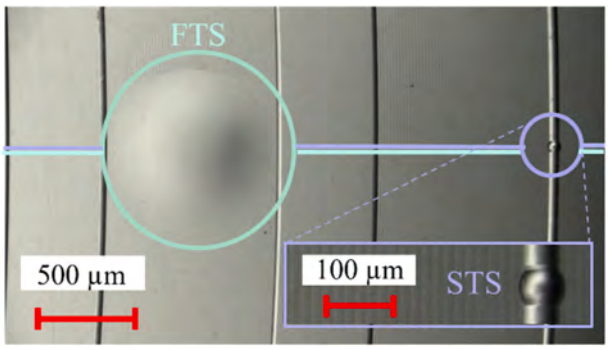

Fig. 18. Enlarged view of the machined surface with time-delay compensation.

4. Results and discussions

4.1. Before time delay compensation

Fig. 14 shows an overall view of the processed sample and an enlarged view of the machined surface observed under a microscope. By comparing the positions of the spherical dimples machined by FTS and STS, it was confirmed that the position of the FTS spherical dimple was visually angularly shifted by a time delay. Fig. 15 shows the form error map of the machined spherical dimples measured using a 3-D profiler. The average peak-to-valley (P–V) values for the spherical dimples of the center, STS, and FTS were 129, 96, and 564 nm, respectively, indicating that ultra-precision cutting was performed. In the form error pattern of the FTS in Fig. 15(c), it was confirmed that a crescent-shaped pattern appeared in the cutting direction in all cases. This was caused by the tool-following error shown in Fig. 10(b), which increased proportionally with the cutting depth.

The angular positions of the spherical dimples machined by STS and FTS were calculated relative to the spherical dimple of STS at 0°, and the amount of shift from the ideal position for each calculated angular position is shown in Fig. 16. The results in Fig. 16(a) indicate that the time delay during machining causes a large angular misalignment in FTS machining, and the average angular shift is 1.149°. A comparison of the FTS and STS plots showed similar plot patterns, as shown in Fig. 16(b) and (c). The time-delay measurement itself was not significantly affected by this plot pattern because similar plot patterns appeared in STS and FTS machining. The causes of the appearance of these sine-wave-like

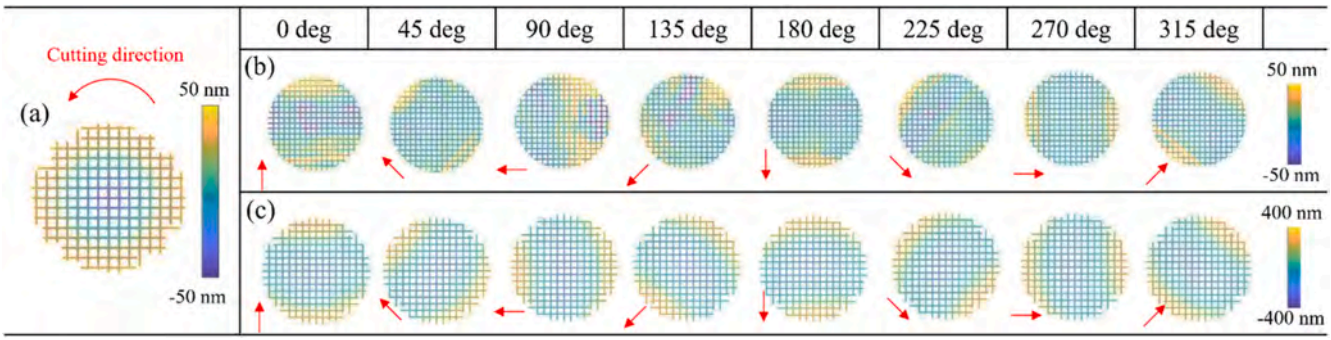

Fig. 19. Form error map of the (a) machined center spherical dimple by STS and eight outer spherical dimples machined by (b) STS and (c) FTS with the proposed time delay compensation.

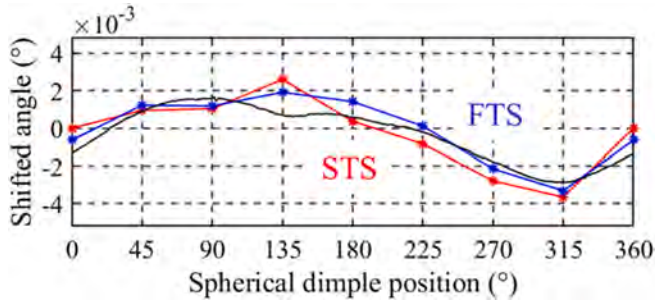

Fig. 20. Measurement results of the shifted angle from the ideal position based on the detected center position of 0 °with time delay compensation and detection error data of the spindle encoder.

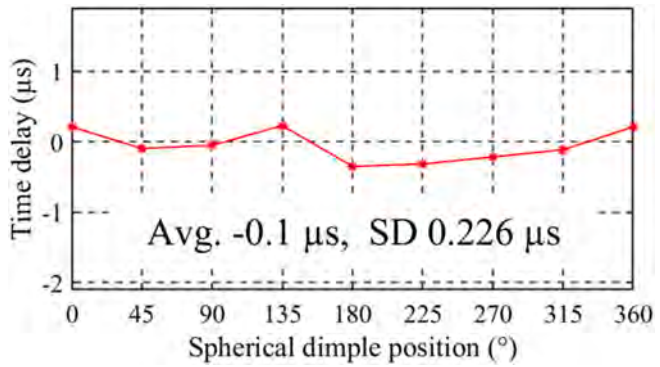

Fig. 21. Time delay calculation results after time delay compensation.

shapes are discussed in Section 4.2.

The angular misalignment of the spherical dimples of each FTS was determined by comparing the angular misalignment with the spherical dimples of the STS at the same angle. The time delay is calculated from the angular misalignment value. The results for the time delays are presented in Fig. 17. The mean value of the acquired time delay was 383.1 μs, with a standard deviation of 0.461 μs. By theoretical calculation and adjustment of parameters related to measurement accuracy, an accuracy of less than 0.5 μs standard deviation was achieved.

4.2. After time delay compensation

The results of the machined surface observed by a microscope are shown in Fig. 18. Compared with Fig. 14, it can be seen that the machining deviation has improved. Fig. 19 shows the form error map for each spherical dimple. The average P–V values were 216, 155, and 517 nm for the spherical dimples of the center, STS, and FTS, respectively. Compared with the experimental results of the FTS dimple spheres before compensation (Fig. 15(c)), there was no significant change (8.3% reduction) in the average P–V values, and a similar crescent-shaped pattern was observed in the form error map after time delay compensation. This result confirms that the proposed compensation process does not affect the deterioration of the machining accuracy.

Fig. 20 shows the results of the angular position deviation of each sphere from its ideal position based on the spherical dimple of STS at 0°. The average angular misalignment of the FTS before compensation was 1.149°; then, it was reduced to 3.47×10^{-4} ° after time delay compensation, confirming the effectiveness of the proposed compensation method for angular misalignment caused by time delay. This result indicates that the machining position error in the rotational direction was reduced to 97 nm from 321 μm (99.97% reduction).

Similar plot patterns were observed for both the STS and FTS results in Fig. 20, as before compensation (Fig. 16(b) and (c)). This plot pattern is considered to be affected by the detection error of the encoder that recognizes the C-axis coordinate value. The spindle encoder error data for diamond turning are shown by the black line in Fig. 20. A comparison of the encoder error data with the measured shifted angle of the spherical dimple in Fig. 16(b) and (c) and Fig. 20 confirms that a similar sine wave-like pattern appears in the detection error of the spindle encoder. From this comparison, the detection error of the spindle encoder is considered to be affected by the plot pattern of the angular deviation measurement results. In this study, to simplify the machining conditions, a correction program for the detection error of the spindle encoder in the diamond turning and FTS was turned off.

Fig. 21 shows the results of the time delay calculation based on the measured angular deviation results. The mean value of the residual time delay after compensation was −0.1 μs, successfully correcting the time delay with an accuracy of less than 1 μs. The experimental results confirm that the proposed measurement and compensation for the time delay is an effective method for improving the angular misalignment caused by the time delay in FTS-based diamond turning.

5. Conclusions

A novel method for measuring the time delay from the actual machined workpiece surface and compensating for the angular misalignment based on the measured time delay was proposed. The main conclusions are summarized as follows:

(1) Precisely measuring the time delay, machining a set of spherical dimples in the workpiece center and outer region of the workpiece using STS and FTS, respectively, and comparing their profiles are effective methods.
(2) Theoretical calculations clarified that the values of the spindle rotation rate, dimple placement position, and center position detection error are related to the time delay measurement accuracy.

(3) The experimental results revealed that the independent FTS unit used in this study had a mean time delay of 383.1 μs and a standard deviation of 0.461 μs.
(4) To compensate for the time delay, an additional program was developed to change the value of the detected C-axis tool position to a time-delayed position. Determining the W-axis coordinate value based on the changed C-axis position value successfully reduced the angular misalignment.
(5) The results after time delay compensation showed that the mean values of the residual time delay and the machining angular deviation were 0.1 μs and 3.47×10^{-4} °, respectively. The machining position error in the rotational direction was successfully reduced from 321 μm to 97 nm.

This study demonstrates the possibility of measuring and compensating for time-delay-induced angular misalignment in FTS turning. The proposed method is expected to improve the accuracy of ultra-precision machining via FTS-based diamond turning and contribute to the advanced manufacturing of optical components. As the time delay varies with cutting conditions, as a future task, the authors will focus on the prediction of time delay from cutting conditions based on the measurement method proposed in this study.

Declaration of competing interest

The authors declare that they have no known competing financial interests or personal relationships that could have appeared to influence the work reported in this paper.

References

[1] Gurganus D, Owen JD, Davies MA, Dutterer BS, Novak S, Symmons A. Precision glass molding of freeform optics. September Freeform Optics 2018;2018:28. https://doi.org/10.1117/12.2320574.
[2] Blalock T, Medicus K, DeGroote Nelson J. Fabrication of freeform optics. Opt. Manuf. Test. XI 2015;9575(August 2015):95750H. https://doi.org/10.1117/12.2188523.
[3] Mishra V, Sabui D, Burada DR, karar V, Jha S, Khan GS. Experimental investigations on slow tool servo process parameters for freeform optics machining. Mater Manuf Process 2020;35(7):797–810. https://doi.org/10.1080/10426914.2020.1743849.
[4] Fang FZ, Zhang XD, Hu XT. Cylindrical coordinate machining of optical freeform surfaces. Opt Express 2008;16(10):7323. https://doi.org/10.1364/oe.16.007323.
[5] Ye J, Chen L, Li X, Yuan Q, Gao Z. Review of optical freeform surface representation technique and its application. Opt Eng 2017;56(11):1. https://doi.org/10.1117/1.oe.56.11.110901.
[6] Zhang Z, Yan J, Kuriyagawa T. Manufacturing technologies toward extreme precision. Int J Extrem Manuf 2019;1(2). https://doi.org/10.1088/2631-7990/ab1ff1.
[7] Song W, Wang Y, Cheng D, Liu Y. Design of light field head-mounted display. Int Opt Des Conf 2014;9293(December 2014):92930J. https://doi.org/10.1117/12.2075183. 2014.
[8] Wang J, Liang Y, Xu M. Design of a see-through head-mounted display with a freeform surface. J Opt Soc Korea 2015;19(6):614–8. https://doi.org/10.3807/JOSK.2015.19.6.614.
[9] Kramida G. Resolving the vergence-accommodation conflict in head-mounted displays. IEEE Trans Vis Comput Graph 2016;22(7):1912–31. https://doi.org/10.1109/TVCG.2015.2473855.
[10] Ottevaere H, et al. Comparing glass and plastic refractive microlenses fabricated with different technologies. J Opt Pure Appl Opt 2006;8(7). https://doi.org/10.1088/1464-4258/8/7/S18.
[11] Harvey JE. Total integrated scatter from surfaces with arbitrary roughness, correlation widths, and incident angles. Opt Eng 2012;51(1):013402. https://doi.org/10.1117/1.oe.51.1.013402.
[12] Zhong K, Zhang H, Gao Y. Fabrication of high fill-factor aspheric microlens array by digital maskless lithography. Optik 2017;142:243–8. https://doi.org/10.1016/j.ijleo.2017.05.069.
[13] Mukaida M, Yan J. Ductile machining of single-crystal silicon for microlens arrays by ultraprecision diamond turning using a slow tool servo. Int J Mach Tool Manufact 2017;115(November 2016):2–14. https://doi.org/10.1016/j.ijmachtools.2016.11.004.
[14] Cheng Y-C, Hsu M-Y, Peng W-J, Hsu W-Y. Fabrication and correction of freeform surface based on Zernike polynomials by slow tool servo. 2017. p. 42. https://doi.org/10.1117/12.2279270. vol. 1044813, no. October 2017.
[15] Scheiding S, et al. Diamond milling or turning for the fabrication of micro lens arrays: comparing different diamond machining technologies. Adv Fabr Technol Micro/Nano Opt Photonics IV 2011;7927(24):79270N. https://doi.org/10.1117/12.874751.
[16] Zhu L, Li Z, Fang F, Huang S, Zhang X. Review on fast tool servo machining of optical freeform surfaces. Int J Adv Manuf Technol 2018;95(5–8):2071–92. https://doi.org/10.1007/s00170-017-1271-4.
[17] Vyboishchik AV. Modelling topology of freeform surfaces with ball-end milling. Procedia Eng 2016;150:761–7. https://doi.org/10.1016/j.proeng.2016.07.103.
[18] Tian F, Yin Z, Li S. Fast tool servo diamond turning of optical freeform surfaces for rear-view mirrors. Int J Adv Manuf Technol 2015;80(9–12):1759–65. https://doi.org/10.1007/s00170-015-7152-9.
[19] Nagayama K, Yan J. Deterministic error compensation for slow tool servo-driven diamond turning of freeform surface with nanometric form accuracy. J Manuf Process 2021;64(November 2020):45–57. https://doi.org/10.1016/j.jmapro.2021.01.015.
[20] Yuan J, Lyu B, Hang W, Deng Q. Review on the progress of ultra-precision machining technologies. Front Mech Eng 2017;12(2):158–80. https://doi.org/10.1007/s11465-017-0455-9.
[21] Hatefi S, Abou-El-Hossein K. Review of non-conventional technologies for assisting ultra-precision single-point diamond turning. Int J Adv Manuf Technol 2020;111(9–10):2667–85. https://doi.org/10.1007/s00170-020-06240-7.
[22] Tian F, Yin Z, Li S. A novel long range fast tool servo for diamond turning. Int J Adv Manuf Technol 2016;86(5–8):1227–34. https://doi.org/10.1007/s00170-015-8282-9.
[23] Kim HS, Kim EJ, Song BS. Diamond turning of large off-axis aspheric mirrors using a fast tool servo with on-machine measurement. J Mater Process Technol 2004;146(3):349–55. https://doi.org/10.1016/j.jmatprotec.2003.11.028.
[24] Kim HS, Kim EJ. Feed-forward control of fast tool servo for real-time correction of spindle error in diamond turning of flat surfaces. Int J Mach Tool Manufact 2003;43(12):1177–83. https://doi.org/10.1016/S0890-6955(03)00156-1.
[25] Liu Q, Zhou X, Liu Z, Lin C, Ma L. Long-stroke fast tool servo and a tool setting method for freeform optics fabrication. Opt Eng 2014;53(9):092005. https://doi.org/10.1117/1.oe.53.9.092005.
[26] Sato Y, Yan J. Tool path generation and optimization for freeform surface diamond turning based on an independently controlled fast tool servo. Int J Extrem Manuf 2022;4(2). https://doi.org/10.1088/2631-7990/ac5f12.
[27] Kong LB, Cheung CF, Kwok TC. Theoretical and experimental analysis of the effect of error motions on surface generation in fast tool servo machining. Precis Eng 2014;38(2):428–38. https://doi.org/10.1016/j.precisioneng.2013.12.010.
[28] Cai HB, Shi GQ. Tool path generation for multi-degree-of-freedom fast tool servo diamond turning of optical freeform surfaces. Exp Tech 2019;43(5):561–9. https://doi.org/10.1007/s40799-019-00307-1.
[29] Yu DP, Gan SW, Wong YS, Hong GS, Rahman M, Yao J. Optimized tool path generation for fast tool servo diamond turning of micro-structured surfaces. Int J Adv Manuf Technol 2012;63(9–12):1137–52. https://doi.org/10.1007/s00170-012-3964-z.